

# Energy landscape and diffusion kinetics of lithiated silicon: A kinetic activation-relaxation technique study

Mickaël Trochet\* and Normand Mousseau†

*Département de physique and Regroupement québécois sur les matériaux de pointe, Université de Montréal, C.P. 6128, Succursale Centre-Ville, Montréal, Québec, Canada H3C 3J7*

(Received 3 August 2017; published 19 October 2017)

With large specific and volumetric capacity, lithiated silicon is an excellent anode for lithium-ion batteries. Its application is challenged today, however, by the formation of an amorphous  $a\text{-Li}_x\text{Si}$  phase associated with a large volume change that occurs at relatively low Li concentration and remains only very partly understood at the microscopic level. In this paper, we characterize the full energy landscape associated with the onset of Li insertion in crystalline Si as a first step for understanding the lithiation process. We identify the diffusion mechanisms and migration energies for one to ten Li atoms in a Si crystal as well as the average lifetime of small lithium aggregates, using the kinetic activation-relaxation technique (kART), an off-lattice kinetic Monte-Carlo method with on-the-fly catalog building capabilities coupled to a newly developed force field (ReaxFF) used as potential based on *ab initio* results. We show that the short lifetimes of the bound states (from meV to ten meV) mean that Li atoms move in the interstitial sublattice with little interactions, explaining how high Li concentration in Si can be reached.

DOI: [10.1103/PhysRevB.96.134118](https://doi.org/10.1103/PhysRevB.96.134118)

## I. INTRODUCTION

Lithium-ion batteries represent the dominant technology for rechargeable energy storage in portable and mobile equipment. As such, they have been the subject of considerable research and development over the last two decades, with significant efforts expanded for identifying new anode materials that could produce longer-lasting, denser, and cheaper batteries. Among the most fascinating materials, silicon-based materials have emerged as potential candidates for anodes as they display a very high theoretical energy capacity— $\text{Li}_{4.4}\text{Si}$  displays a 4200 mAh/g capacity, ten times higher than graphite (372 mAh/g) [1–3] and slightly higher than metallic Li 3860 mAh/g [4].

This exceptional capacity is, however, counterbalanced by a low intrinsic electrical conductivity and, more challenging, very poor cycling performance associated with a large volume expansion associated with the creation of an amorphous structure at room temperature [5,6] causing important structural damages to the Si anode and drastically reducing its real-life capacity [7,8]. While this behavior was first observed 15 years ago [5,9,10], the mechanisms leading to this expansion as well as the associated atomic conformations are still largely unknown. Surprisingly, the structure evolution of the lithiation of c-Si anode is observed to start at the surface as soon as Li inserts into the Si anode [6,11–13], with the formation of an amorphous  $a\text{-Li}_x\text{Si}$  phase, where  $x \approx 3.5$ .

The cycling limitation can be lifted, however, through the use of Si nanostructures [14–18] and thin films [19–22] for lithium battery anodes. While early amorphous silicon films show poor cycling ability (from 1000 mAh/g to 200 mAh/g at C/2 rate) [19], Ohara [20] successfully improved this property by controlling Si films thickness and doping, maintaining a 3200 mAh/g capacity, with less than 1% loss over 1000 cycles,

at 12C rates for a 500 Å thick film of n-type conductive Si. Amorphous silicon nanowires have also been found to procure significant advantages, ensuring, for example, that the large volume expansion is evenly distributed, preventing fractures that can occur in c-Si while maintaining a high charge storage capacity from 2400 mAh/g with 10% loss over 30 cycles at C/5 rate [18]. Understanding the effect of microstructures is essential to improve the cycle life of this kind of Si anode.

To understand how amorphization takes place in these systems, it is essential to detail Li-Li and Li-Si interactions. In this paper we focus on the very onset of Li insertion in Si in order to characterize the associated energy landscape and clustering mechanisms. We focus, more specifically, on the diffusion and clustering of 1 to 10 Li atoms in crystalline Si. For this, we use the kinetic activation-relaxation technique (k-ART), an off-lattice kinetic Monte-Carlo algorithm with on-the-fly cataloging capacities that fully incorporates short and long-range elastic effects and that has been applied with success to follow atomistic evolution of complex materials over a time scale of 1 second and more [23–26]. K-ART is coupled with a recently proposed ReaxFF parameter set for Si-Li [27] to allow the study of sufficiently large boxes.

After presenting the methodology used here, we characterize the energy landscape and diffusion mechanisms for 1, 2, 3, and 10 Li interstitials in a 4096-Si box. We then identify the cluster structures that lead to pinning and discuss the onset of lithiation. We find, in particular, that average lifetime of bound compound for two to four Li clusters at 300 K are on the order of millisecond, similar to their diffusion time. Li atoms therefore interact only very weakly as they move through Si, facilitating its insertion at high concentration.

## II. METHODS

### A. Kinetic ART

All simulations presented here are performed using the kinetic activation relaxation technique [28,29]. This algorithm

\*mickael.laurent.trochet@umontreal.ca

†normand.mousseau@umontreal.ca

introduces three significant improvements over standard kinetic Monte Carlo (KMC) [30,31] in order to treat correctly the kinetics of complex materials.

To allow off-lattice motion, one of the main limitations of standard KMC, k-ART introduces a topological classification using NAUTY [32] for both local environment and events. This approach makes it possible to handle with the same ease both crystalline and disordered states, as well as interfaces, surfaces, and alloys. K-ART also uses the efficient ART nouveau algorithm [33,34] to identify on-the-fly events associated with new environments, reducing the amount of computation to be performed at the onset of the simulation. This approach ensures that events associated with new atomic states are fully considered, without overloading the catalog with conformations that will never be visited. Finally, short and long-range elastic deformations are computed exactly by reconstructing and reconverging all relevant transition state energies at every step.

While the k-ART algorithm is described in more details in previous publications [28,29,35–38], we present here a brief description of its implementation. After a k-ART step, the local topology of each atom is reassessed using the topological analysis package NAUTY [32]. For this, all atoms within a certain radius surrounding an atom (here: 6 Å) are selected as vertices of a graph. Edges are drawn between atoms separated by less than a first neighbor cutoff (here: 2.8 Å). The automorphic group of the resulting graph is then computed, providing a unique identifier and sufficient information to recover permutations and symmetry operations between two automorphic configurations.

All atomistic environments belonging to the same automorphic group are considered to share a common list of events. This hypothesis can be verified at the event-reconstruction stage. When it fails, new cutoffs are introduced, to ensure a unique correspondence between topology and geometry. After each k-ART move, event searches are launched for all newly identified topologies. A few extra event searches are also performed for common configurations using ART nouveau, an efficient open-ended transition state finding algorithm [33,34,39].

Topology keys are computed for all local configurations generated during the event search and are associated with local minima and first-order transition states. Identified topologies are the set of all local minima generated during a simulation while visited topologies refer to the set of different topologies on the kinetic path corresponding to the system's evolution.

Twenty five independent and random ART nouveau searches are launched for each new topology. An event is defined as an ensemble of three configurations: initial local minimum, saddle point, and final local minimum.

In the Li-Si system, k-ART typically finds an average of three to four different events with an activation energy below 5 eV per topology. Once the event catalog is updated, events are ordered as a function of their rate, computed using transition state theory, with a constant prefactor of  $10^{13}$  Hz. Events within 99.99% of the total ascending cumulative rate are fully reconstructed and their transition state is relaxed to a precision of  $0.02 \text{ eV Å}^{-1}$ , to take into account all elastic and geometric particularities, leading to an energy precision for each specific

saddle point energy of 0.01 eV or better. Following standard KMC [30], a time step is computed according to:

$$\Delta t = -\ln(\mu) / \sum_i r_i, \quad (1)$$

where  $\mu$  is a random number uniformly distributed between 0 and 1 and  $r_i$  is the transition rate of event  $i$ ; an event is then selected with a probability proportional to its relative weight.

Flickering states, i.e., states of similar energy separated by a relatively low activation energy that do not lead to diffusion, are handled using the basin-accelerated mean-rate method (bacMRM) [29] based on the mean rate method (MRM) of Puchala *et al.* [40]. As connected flickering states are discovered, they are added into a basin. The basin's internal kinetics are solved directly and exit rates are corrected for the internal motion. This minimizes the computational efforts of handling the nondiffusive motion while ensuring correct kinetics. Finally, the average time of exit basin  $\sum_k \langle \tau_k \rangle$  is used as KMC step in the current implementation of kART.

## B. Force fields

Force fields are obtained from the large-scale atomic/molecular massively parallel simulator (LAMMPS) [41] through the coupling of its library to k-ART, providing access to a very large catalog of well-tested and efficiently programmed force fields. To accelerate the computation, a double parallelization allows both event generation and force calculations on multiple processors [38]. In the present study, we use the reactive force field (ReaxFF) [42] with the LiSi parameters developed by Fan *et al.* [27].

## C. Simulated systems

### 1. Input parameters chosen

We characterize the diffusion pathways of lithium interstitials in a crystalline box of 4096 Si atoms with periodic boundary conditions. For each system, containing between one to four and 10 Li interstitials, we perform runs at 300 K. For the system with only one Li, we consider three different initial states: interstitial, substitutional, and antisite. We test that this box is large enough to ensure convergence by comparing the local minimum and activation energies for the mono-Li and the di-Li systems with a 8000-atom box (at constant density), finding a maximum of 0.001 eV energy difference for an overall error on relative energies of at most 0.002 eV.

The length of each run is set as a function of the system's kinetics and complexity. Li-interstitials are created by adding Li atoms in octahedral sites. In all cases, the simulation box is a cubic box with a length of 43.44 Å, corresponding to a lattice parameter of 5.43 Å in agreement with the literature for the Si diamond structure at 300 K). The system's energy is first minimized at  $T = 0$  K before k-ART simulations are launched at 300 K.

### 2. Analysis

The formation energy, i.e., the energy cost to remove  $N_{Li}$  Li atoms from the pure Li bcc crystal and insert them in the Si bulk of  $N_{Si}$  Si atoms, is defined as

$$E_f^{\text{conf}} = E^{\text{conf}} - (N_{Si}^{\text{conf}} \varepsilon_{Si} + N_{Li}^{\text{conf}} \varepsilon_{Li}) \quad (2)$$

TABLE I. Comparison of formation ( $E_f$ ) and activation ( $E_a$ ) energies for different configuration of the mono-Li interstitial obtained by different groups using density functional theory (DFT) and various methods for identifying the activation energies: the nudged elastic band method (NEB) or molecular dynamics (MD). The experimental value for the migration energies of lithium diffusion is between 0.57 eV and 0.79 eV [44]. Energies are in eV.

	Our work k-ART (ReaxFF)	Literature DFT or MD
$E_f^{1-LiTd}$	-0.973	-1.42[45] (DFT) -1.359[46] (DFT)
$E_f^{1-LiSub}$	3.22	1.17[45] (DFT) 3.09[47] (DFT) 6.602[46] (DFT)
$E_f^{1-LiAnti-site}$	4.18	2.392[46] (DFT) 4.05[47] (DFT) 0.52[46] (DFT) 0.58[46] (DFT/NEB) 0.58[48] (MD/REAXFF) 0.60[49] (DFT) 0.61[45] (DFT/NEB)
$E_a^{Td-Hex-Td}$	0.520	
$E_a^{1-LiSub}$	2.02	
	0.35	
	1.93	
$E_a^{1-LiAntisite}$	2.26	
	2.63	
	2.87	

where  $E^{conf}$  is the system's total energy, and  $N_{Si}^{conf}$  and  $N_{Li}^{conf}$  the number of Si and Li atoms, respectively.  $\varepsilon_i$  is the per atom cohesive energy calculated for the perfect crystal systems for species  $i$ . Here we use ReaxFF's cohesive energy:  $\varepsilon_{Li} = -1.63$  eV as obtained from a 1024 Li bcc crystal, in excellent agreement with the literature ( $-1.63$  eV [43]) while  $\varepsilon_{Si} = -4.756$  eV is measured from a 4096 Si diamond crystal, in good agreement with the literature ( $-4.63$  eV [43]). For each result, we give the formation energy of the lowest energy state found in the current system then we compare other metastable states according to this lowest energy state which is set to 0.

The binding energy for various clusters is defined as:

$$E_b^{x-mer} = E_f^{x-mer} - N_{y-mer} E_f^{y-mer}, \quad (3)$$

where the number of defects in the y-mer is smaller than in the x-mer. For example, the binding energy of the Li dimer is

$E_b^{dimer} = E_f^{dimer} - 2E_f^{monomer}$ . The sign of the binding energy determines the thermodynamic stability of different bound compound according to the monomers at infinite distance.

### III. RESULTS

In this section, we characterize the various configurations associated with a Li impurity in a box of Si and then describe the structure and stability, the dominant state, and the diffusion mechanism for systems containing one to four and 10 lithium interstitials.

#### A. Comparison with the state of the art

Table I summarizes energies of minima and saddle points for various configurations associated with a single lithium atom impurity in crystalline Si and compares our results to previously reported results for the formation and activation energies of these various states. At  $-0.97$  eV, the Reaxff formation energy for the Li interstitial is 0.4 eV above DFT predictions ( $-1.42$  or  $-1.36$  eV, depending on the source). The migration energy for the ground state transition, associated with the motion of the Li interstitial from one tetrahedral site to another through a hexagonal site, is, however, in good agreement with DFT and experiment, at 0.52 eV.

More energetic defects, such as the Li in substitutional and antisite configurations, with the Si positioned in a neighboring tetrahedral interstitial site, also show generally good agreement with Morris *et al.* DFT calculations [47], that differ significantly from Wan *et al.* [46] and Malyi *et al.* [45]. Since in the absence of Li formation energies of self-interstitial configuration is of the order of 3.31 eV [50], the energy cost of creating an antisite configuration should be higher than a substitutional configuration, supporting Morris *et al.*'s DFT calculations as well as our work.

For Li in substitution, we find only one type of event that involves a concerted motion leading to the formation of two IV pairs composed of the initial substitutional Li and one of the four neighboring Si, 1.79 eV above the initial configuration. While the presence of a Li decreases significantly the activation energy associated with the formation of this defect, with an activation energy of 2.02 eV compared to 4.75 eV [51,52] for the perfect Si crystal, this defect is unstable, with an inverse activation energy of 0.21 eV, and will generally anneal before the vacancy or the Si interstitial can diffuse.

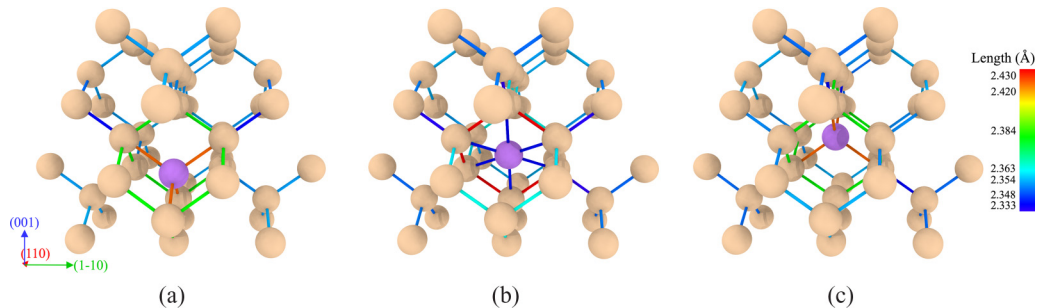


FIG. 1. Diffusion mechanism for 1-Li $T_d$  in c-Si. (a) Initial state: 1-Li $T_d$  states.  $E_f = -0.973$  eV. (b) Saddle point state: hexagonal position.  $E_a = 0.52$  eV. (c) Final state: 1-Li $T_d$  states.  $E_f = -0.973$  eV.

TABLE II. Formation ( $E_f$ ) (top line) and activation energies connecting the three dominant states for the mono-Li-interstitial complex. Values in parenthesis represent events found in the catalog but not executed during simulation. Energies are in eV.

To	From		
	Td	IV pair+1-Li <sub>(1)</sub>	IV pair+1-Li <sub>(2)</sub>
$E_f$	-0.973	0.777	1.187
Td	0.520	(0.23)	(0.11)
IV pair+1-Li <sub>(1)</sub>	(2.00)		
IV pair+1-Li <sub>(2)</sub>	(2.29)		

For the antisite configuration, we find four different transitions involving primarily the Li atom, with activation energies between 1.93 eV and 2.87 eV (see Table I) leading to unstable configurations, with inverse activation energies between 0.05 eV and 0.32 eV. Three of these transitions correspond to the transition observed in the substitutional case (formation of two IV pairs) where the interstitial Si atom is only weakly affected. The fourth transition, with an activation energy of 2.87 eV, corresponds to the positioning of the substitutional Li in adjacent tetrahedral empty site, creating a IV pair.

A transition centered on the Si interstitial is also found with an activation energy of 0.35 eV. This transition represents the motion of the Si interstitial from one tetrahedral site to another through a hexagonal site, only 0.01 eV above the ground state, moving away from the Li that remains in its initial substitutional site.

## B. Monointerstitial

A k-ART run for the Li monointerstitial is launched from an initial configuration consisting of one isolated Li atom placed in a tetrahedral site of the silicon crystal and run for 389 KMC steps, representing 6.37 ms of simulation time. The ground state of the Li monointerstitial system places the impurity in a tetrahedral (Td) site, with a formation energy of  $E_f^{1\text{-Li}_{Td}} = -0.973$  eV. Local lattice deformations are almost nonexistent around the lithium atom: The distance between the interstitial Li and its nearest-neighbor Si atoms is  $d_{\text{Li-Si1}} = 2.420(1)$  Å, only 0.07 Å longer than the equilibrium Si-Si distance, in agreement with the 2.44 Å predicted by DFT [45].

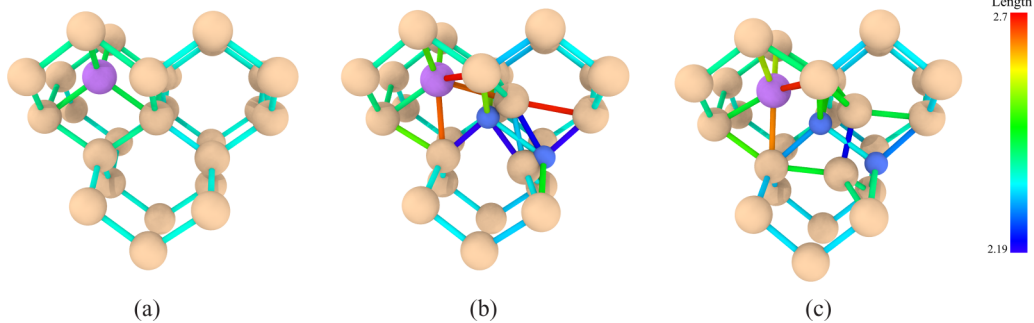


FIG. 2. 2 IV pairs formation with 1-Li<sub>(1)</sub>. Beige: Si atoms; purple: Li; blue: empty Si sites. (a) Initial state: 1-Li<sub>Td</sub> states.  $E_f = -0.973$  eV. (b) Saddle point state.  $E_a = 2.00$  eV. (c) Final state: 2 IV pairs+1-Li<sub>(1)</sub>,  $E_f = 0.777$  eV.

The nearest-neighbor jump through the hexagonal (Hex) site (four equivalent directions), illustrated in Fig. 1, requires crossing a 0.52 eV activation energy, in agreement with DFT and experiments as discussed previously. Averaging the square displacement of the single lithium over the 389 KMC steps, we find a Li diffusivity in Si bulk at 300 K of  $D = 2.47 \times 10^{-12}$  cm<sup>2</sup> s<sup>-1</sup>. Since the diffusion mechanism is a one step process, the migration energy is equal to the Td-Hex-Td activation energy leading to a prefactor of  $D_0 = 2.67 \times 10^{-3}$  cm<sup>2</sup> s<sup>-1</sup>, in agreement with experiment [44] from  $1.9 \times 10^{-3}$  to  $3.8 \times 10^{-3}$  cm<sup>2</sup> s<sup>-1</sup>, which supports our choice of an attempt frequency of  $10^{13}$  Hz.

For a single Li interstitial, k-ART identifies 25 topologies, including topologies centered on the Li and on the Si atoms, and visits eight of them during the simulation. All visited topologies are associated with the Li in Td state, the only one visited during the simulation. From this state, k-ART finds 25 events that correspond to three different transitions along various directions.

Table II summarizes the properties of the three transitions found by ART nouveau associated with these events. The first transition corresponds to the Li Td-Hex-Td jump, from ground state to ground state. The two others lead to the formation of a two interstitial-vacancy pair of Si with the Li in first or second nearest-neighbor position, denoted, respectively, as 2 IV pairs+1-Li<sub>(1)</sub> (see Fig. 2) and 2 IV pairs+1-Li<sub>(2)</sub>. As expected, these IV pairs at 300 K do not form spontaneously as their average time of formation are  $4 \times 10^{20}$  s and  $3 \times 10^{25}$  s, respectively, 25 to 30 orders of magnitude longer than the  $5 \times 10^{-5}$  s for the Li diffusion.

## C. Di-interstitial

### 1. Structure and stability

A k-ART simulation with two Li interstitials is launched from an initial configuration with the two Li atoms positioned in adjacent tetrahedral sites and run for 1226 KMC steps, representing 8.76 ms of simulated time. Since binding energies and elastic deformations are small for this system, we ensure that the bound compound is sampled by starting from the ground state. With Li atoms moving between tetrahedral interstitial sites, di-lithium configurations are labeled as 2-Li<sub>(i)</sub> where  $i$  is the distance in lattice-site spacings between the two Li.

After minimization, the ground, or dimer, state, 2-Li<sub>(1)</sub>, is obtained with a formation energy of  $E_f^{\text{dimer}} = -2.004$  eV

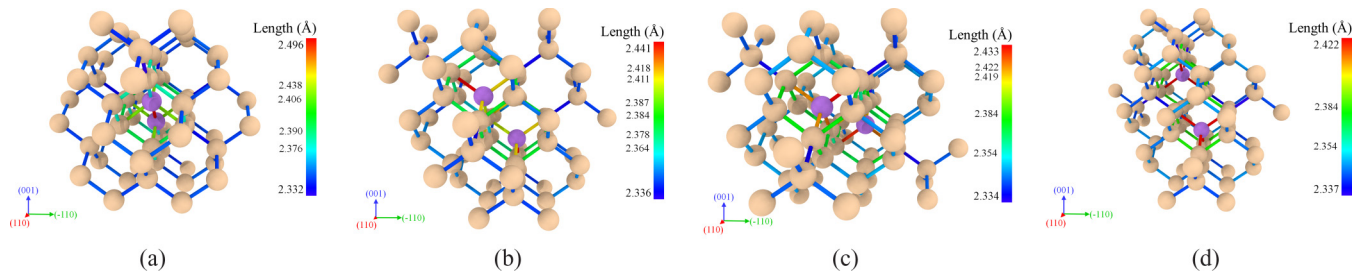


FIG. 3. Representation of the dominant states for 2-Li in c-Si. Bond lengths are displayed according to the scale on the right of each panel. Beige: Si atoms; purple: Li. (a) State dimer  $E_f = -2.004$  eV;  $E_b = -0.057$  eV. (b) State 2-Li<sub>(2)</sub>  $E_f = -1.978$  eV;  $E_b = -0.031$  eV. (c) State 2-Li<sub>(3)</sub>  $E_f = -1.959$  eV;  $E_b = -0.012$  eV. (d) State 2-Li<sub>(4)</sub>  $E_f = -1.956$  eV;  $E_b = -0.009$  eV.

in agreement with Malý *et al.* [45] result ( $-2.43$  eV) or  $-1.002$  eV per Li atom, leading to a binding energy of  $E_b^{\text{dimer}} = -0.057$  eV corresponding to only  $\simeq 2.2k_B T$  at 300 K. In this state, the two Li are on adjacent tetrahedral sites separated by  $d_{\text{Li-Li}} = 2.50$  Å, only slightly deforming the crystalline lattice characterized by a Si-Si distance of 2.35 Å.

While the binding energy calculation here is near that obtained from *ab initio* calculations [45,46,49], which varies from 0.1 to 0.488 eV, the sign of the interaction is different: while we find a weak attraction, DFT calculations predict that two Li atoms slightly repel. This DFT result is surprising since the amorphization of the lattice occurs with a very low concentration of Li, suggesting that Li atoms must attract to increase the local effective concentration [6,11–13], in agreement with ReaxFF's description. Since published DFT predictions for Li-Li interactions were calculated on very small cells, 64 to 216 atoms, elastic and electrostatic size effects would be sufficient to change these energies by a few tenths of eV, sufficient to change the sign of the binding energy.

## 2. Details of the energy landscape

K-ART identifies 128 topologies and visits 30 of them during the simulation. These topologies are associated with

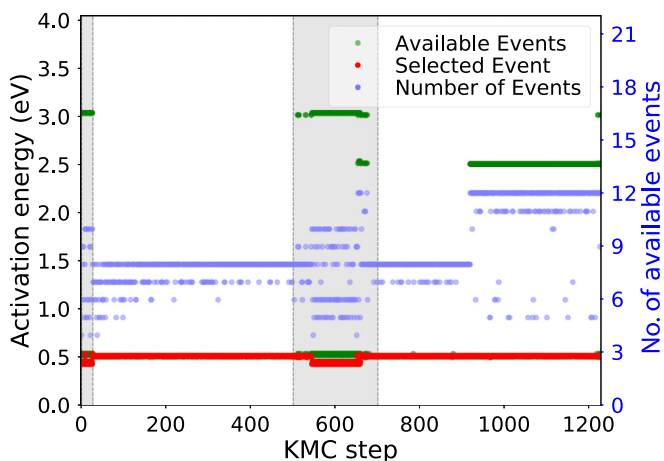


FIG. 4. Evolution of the energy landscape associated with Li atoms only as a function of KMC steps for the two-Li-atom system. Left axis: activation energy for the available (green symbols) and selected (red symbols) events. Right axis: number of available activation energies per KMC steps (blue symbols). Grayed regions indicate the presence of a di-Li bound state.

seven states, with the two Li positioned at various distances from each other, from 2-Li<sub>(1)</sub> to 2-Li<sub>(5)</sub> and 1-Li<sub>Td</sub> with the four first states illustrated in Fig. 3. Because of the cutoff for the topological construction, all configurations where the two Li are further than 6 Å show the same list of topologies. The bound compound represent the collection of states from 2-Li<sub>(1)</sub> to 2-Li<sub>(4)</sub>.

At 0.024 ms (KMC step 26), the bound compound dissociates and the two monomers diffuse freely up to 3.9 ms (KMC step 543) where the bound compound is reforms, lasting 0.18 ms (from KMC step 543 to 659). Figure 4 shows selected and available activation energies as a function of KMC step as well as the number of event in catalog per step for events involving the Li atom. Figure 5 presents the energy landscape

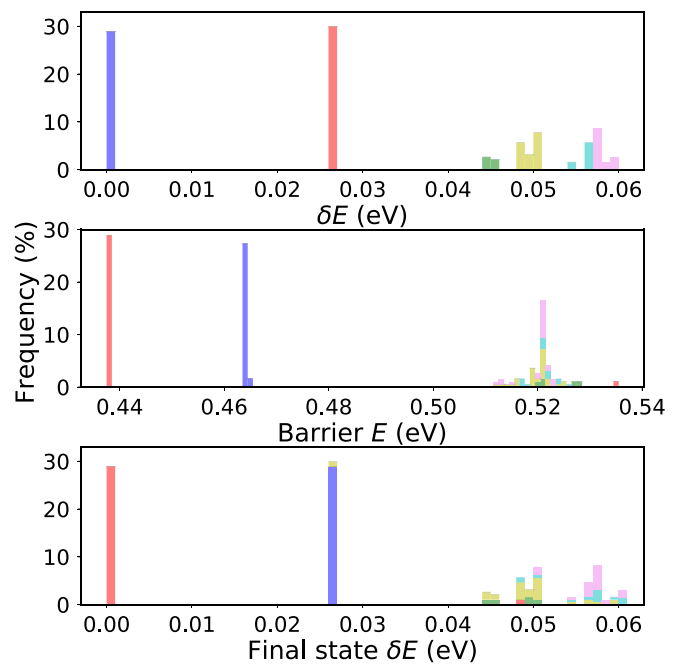


FIG. 5. Evolution of the di-Li system in a bound state (KMC steps 500 to 700). Top panel: energy histogram for the initial states with  $\delta E$  measured from the ground state set at 0.0 eV. Middle panel: histogram of the corresponding activation energies. Bottom panel: energy histogram of the final states. Initial states are color coded: 2-Li<sub>(1)</sub> in blue, 2-Li<sub>(2)</sub> in red, 2-Li<sub>(3)</sub> in green, 2-Li<sub>(4)</sub> in yellow, and 2-Li<sub>(5)</sub> or higher in cyan and purple. Colors are propagated throughout the activation energy and the final state histograms.

TABLE III. Details of the energy landscape for the two Li-atom system. Top three lines: distance between the two Li atoms, formation and binding energies ( $E_f$ ,  $E_b$ ). Bottom part: activation energies for pathways between the six dominant states for the Li di-Li complex. Multiplicity of transition is indicated in parenthesis where A and B labels differentiate between the two Li atoms. Energies and distances are in eV and Å, respectively.

To \ From	dimer	2-Li <sub>(2)</sub>	2-Li <sub>(3)</sub>	2-Li <sub>(4)</sub>	2-Li <sub>(5)</sub>	2-Li <sub>(6)</sub>
Distance	2.50	3.83	4.53	5.44	5.92	6.66
$E_f$	-2.004	-1.978	-1.959	-1.956	-1.947	-1.944
$E_b^{2\text{-Li}} = E_f - 2E_f^{Td}$	-0.057	-0.031	-0.012	-0.009	0	+0.003
dimer		0.438 (1A,1B)				
2-Li <sub>(2)</sub>	0.464 (3A,3B)		0.524 (2A,2B)		0.52(2A,2B)	
2-Li <sub>(3)</sub>		0.543 (2A,2B)		0.53 (2A,2B)		0.518 (1A)
2-Li <sub>(4)</sub>			0.54 (1A,1B)			
2-Li <sub>(5)</sub>		0.523 (1A,1B)				0.52 (2B)
2-Li <sub>(6)</sub>			0.53 (1A,1B)		0.52(2A,2B)	
2-Li <sub>(7)</sub>				0.511 (2A,2B)		0.52 (1A,1B)
2-Li <sub>(8)</sub>					0.52(1A,1B)	
2-Li <sub>(9)</sub>						0.52 (2A)
2-Li <sub>(10)</sub>						
2-Li <sub>(11)</sub>						0.52 (1B)

for the bound di-Li compound. Configurations are color coded from the initial local minimum and the color propagates throughout the activation energy histogram (middle panel) and the final local minimum histogram (bottom panel).

The bound compound, composed of the GS and 2-Li<sub>(2)</sub> (see Fig. 3 and Table III), can diffuse by oscillating between these two states crossing alternating activation energies of 0.46 eV and 0.44 eV. This move represents 60% of the selected events between KMC steps 500 and 700 as shown in Fig. 5.

Table III summarizes the energy landscape for the di-Li bound compound, providing information regarding formation, binding, and transition energies for states with the Li atoms in 1st to 6th nearest neighbor positions along with the multiplicity of each transition. With six identical pathways leading from the GS to 2-Li<sub>(2)</sub>, the compound can move in any direction. From 2-Li<sub>(2)</sub>, however, only two saddle point states, out of six, bring the system back into the GS: each Li can jump to one of four available neighbor sites, but only one leads to the GS; two other transitions for each Li bring the system in 2-Li<sub>(3)</sub> with an activation of 0.54 eV and the last one, in 2-Li<sub>(5)</sub> with an activation energy of 0.52 eV. Configurations for Li in first to fifth neighbor show the same event list for the two Li. This symmetry breaks only for the atoms in sixth nearest neighbor position where a transition from 2-Li<sub>(6)</sub> to 2-Li<sub>(3)</sub> can take place for only one Li due to the relative orientation of the two tetrahedrons formed by each Li atom.

### 3. Average lifetime of the di-Li bound compound

The maximum diffusivity for the Li dimer, calculated using the oscillation between the GS to 2-Li<sub>(2)</sub>, is  $D = 3.69 \times 10^{-10} \text{ cm}^2 \text{ s}^{-1}$ , two order of magnitude higher than for the single Li, suggesting that the dimer could play an important role in diffusing Li through Si.

To assess this role, it is necessary to also evaluate the lifetime of this compound. This is straightforward as k-ART provides complete information regarding the energy landscape for the di-Li system.

Defining the bound compound as consisting of the four closest states shown in Fig. 3 and the escaping states as 2-Li<sub>(5)</sub>, 2-Li<sub>(6)</sub>, 2-Li<sub>(7)</sub> states, we use the Mean Rate Method to find a lifetime of 65.4  $\mu\text{s}$ . Since the timescale associated with the displacement from GS to GS is about 0.99  $\mu\text{s}$ , at 300 K, the di-Li bound compound diffuse for 65 steps on average before dissociating.

## D. Tri-interstitial

### 1. Structure and stability

A k-ART simulation is launched from an initial structure with three Li atoms placed in adjacent interstitial tetrahedral sites in the Si crystal and run for 682 KMC steps, representing 2.43 ms of simulation time. The various visited states are labeled 3-Li<sub>(i,j,k)</sub>, where {i,j,k} refers to the the relative position of each pair in terms of lattice distance. Since the three Li atoms are identical, the {i,j,k} triplet is sorted in ascending order.

After minimization on the first KMC step, the ground state, 3-Li<sub>(1,1,2)</sub> (or trimer), is reached with a formation energy of  $E_f^{\text{trimer}} = -3.014 \text{ eV}$ . Comparing the binding energies of the tri-Li system with both previous systems, we find :  $E_b^{\text{trimer}} - 3E_b^{1\text{-Li}Td} = -0.094 \text{ eV} (\simeq 3.6 k_B T)$  and  $E_b^{\text{trimer}} - E_b^{\text{dimer}} - E_b^{\text{monomer}} = -0.037 \text{ eV} (\simeq 1.4 k_B T)$ .

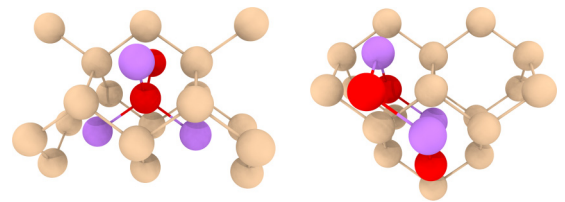


FIG. 6. Representation of the 3-Li<sub>(2,2,2)</sub> (left) trigonal and (right) ring states. Li occupied and empty sites are displayed in purple and red, respectively. Si atoms are represented in beige.

TABLE IV. Details of formation, binding, and activation energies for the three Li-atom system, including relative ( $\delta E$ ), formation ( $E_f$ ), and trimer binding ( $E_b^3 = E_f - 3E_f^{1-LiTd}$ ,  $E_b^{1+2} = E_f - E_f^{1-LiTd} - E_f^{2-Li(0)}$ ) energies and, in the bottom part, the activation energies for events between the 10 dominant states for the Li trimer complex. Multiplicity of transition are indicated for each atom (A, B, and C) in parenthesis. White and green entries correspond to the trimer class, red entries correspond to the dimer+monomer class, and blue entries corresponds to monomers class. Energies are in eV.

From To	3-Li(1,1,2)	3-Li(1,2,5)	3-Li(2,2,2) Trigonal	3-Li(1,2,3)	2-Li(1) & 1-LiTd	3-Li(2,2,2) Ring	2-Li(2) & 1-LiTd	2-Li(3) & 1-LiTd	2-Li(4) & 1-LiTd	3 × 1-LiTd
$\delta E$	0	0.001	0.005	0.013	0.036	0.047	0.063	0.082	0.085	0.094
$E_f$	-3.014	-3.013	-3.009	-3.001	-2.978	-2.967	-2.951	-2.932	-2.929	-2.920
$E_b^3 = E_f - 3E_f^{1-LiTd}$	-0.094	-0.093	-0.089	-0.081	-0.058	-0.047	-0.031	-0.012	-0.009	0.000
$E_b^{1+2} = E_f - E_f^{1-LiTd} - E_f^{2-Li(0)}$	-0.037	-0.036	-0.031	-0.024	0.000	0.010	0.026	0.045	0.048	0.057
number of transitions in INN jumps	(3A,2B,3C)	(3A,3B,4C)	(4A,4B,4C)	(3A,3B,4C)	(3A,3B,4C)	(4A,4B,4C)	(4A,4B,4C)	(4A,4B,4C)	(4A,4B,4C)	(4A,4B,4C)
3-Li(1,1,2)		0.454 (1C)	0.380 (1A,1B,1C)	0.463 (1C)						
3-Li(1,2,5)	0.455 (1A,1C)	0.393 (1B)								
3-Li(2,2,2) Trigonal	0.385 (2B)									
3-Li(1,2,3)	0.476 (2A,2C)			0.405 (1B) 0.560 (1C)						
3-Li(1,3,4)		0.547 (2C)		0.540 (1C)						
3-Li(1,3,6)				0.513 (1C)						
3-Li(1,5,6)				0.495 (1A)						
3-Li(2,2,4)				0.443 (1A)						
3-Li(2,2,6)		0.463 (2A)								
3-Li(1,5,8)		0.531 (1C)								
3-Li(2,2,8)		0.465 (1A)								
2-Li(1) & 1-LiTd					x		0.438			
3-Li(2,3,5)										
3-Li(2,3,3)										
3-Li(2,2,2) Ring						x				
2-Li(2) & 1-LiTd							x	0.524		0.52
2-Li(3) & 1-LiTd							0.543	x	0.53	0.518
2-Li(4) & 1-LiTd								0.54	x	0.502
3 × 1-LiTd								0.53	0.511	0.52

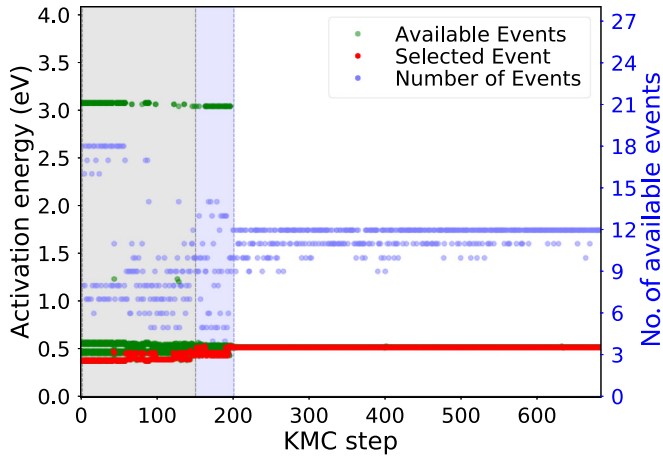


FIG. 7. Evolution of the energy landscape associated with Li atoms only as a function of KMC steps for the three-Li-atom system. Left axis: activation energy for the available (green symbols) and selected (red symbols) events. Right axis: number of available activation energies per KMC steps (blue symbols). The gray and blue region indicated the presence of tri-Li and di-Li bound compounds, respectively.

These allow us to group all observed states into three classes of various stability. First, the compact states, with a binding energy generally below  $-0.06$  eV. This class counts at least 14 states with five dominant ones:  $3\text{-Li}_{(1,1,2)}$ ,  $3\text{-Li}_{(1,2,5)}$ ,  $3\text{-Li}_{(1,2,3)}$ , and two  $3\text{-Li}_{(2,2,2)}$  states: a trigonal conformation with an empty tetrahedral site in the center of the complex and a ring conformation where the center of the complex is occupied by two Si atoms (see Fig. 6), which creates a local constraint largely responsible for the 40 meV energy difference between the trigonal and ring states as reported in Table IV. The second class corresponds to the di-Li bound compound with an isolated mono Li which is characterized by the binding energy interval between  $-0.06$  eV and  $0.0$  eV. The third class corresponds to the three unbound Li.

Table IV displays the binding energies for ten states which are the most frequently observed. K-ART identifies 689 different topologies and visits 47 of them during the simulation. For the first 0.12 ms (200 KMC steps), the system evolves between the tri-Li and di-Li bound compound. At 0.05 ms (KMC step 152), one Li breaks apart and diffuses separately from the di-Li complex (see Figs. 7 and 8). At 0.12 ms (KMC step 200) the di-Li complex also breaks apart. In the absence of strong elastic deformation, Li atoms are not attracted to each other and never come closer than  $8.03$  Å (corresponding to the ninth NN position) for the rest of the simulation (2.43 ms).

## 2. Diffusion and lifetime

There are two main diffusion processes for the ground state  $3\text{-Li}_{(1,1,2)}$ . The first process is a three-step mechanism corresponding to a translation along the  $\langle 110 \rangle$  direction (Fig. 9): From  $3\text{-Li}_{(1,1,2)}$ , a Li atom jumps to  $3\text{-Li}_{(1,2,5)}$  state by crossing an activation energy of  $E_a = 0.455$  eV, a second Li atoms moves, corresponding to an overall translation of the  $3\text{-Li}_{(1,2,5)}$  cluster with an activation energy of  $E_a = 0.393$  eV; the final step brings the cluster into the ground state with

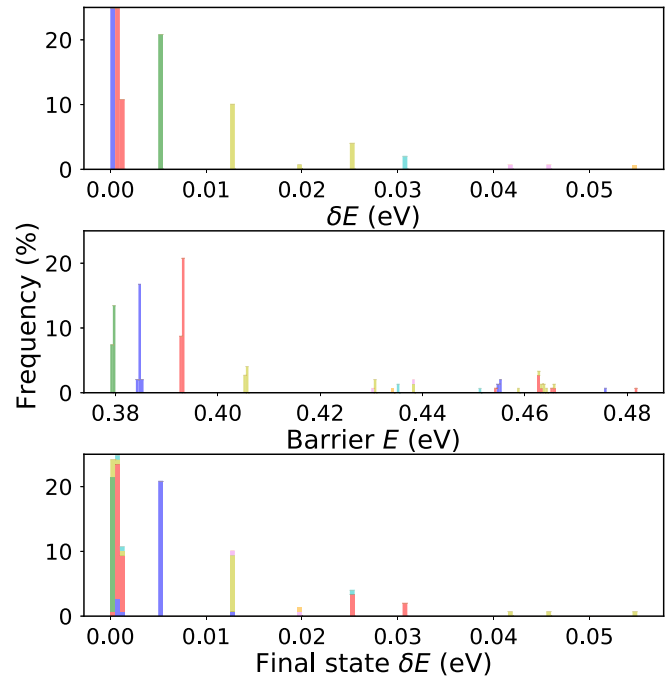


FIG. 8. Evolution of the di-Li system in a bound state (first 150 KMC steps). Top panel: energy histogram of the initial states with  $\delta E$  measured from the ground state set at  $0.0$  eV. Middle panel: histogram of the corresponding activation energies. Bottom panel: energy histogram of the final states. Initial states are color coded. Blue: trimer  $3\text{-Li}_{(1,1,2)}$ ; red:  $3\text{-Li}_{(1,2,5)}$ ; green:  $3\text{-Li}_{(2,2,2)}$  ring; first yellow bin at  $0.013$  eV:  $3\text{-Li}_{(1,2,3)}$ ; cyan: dimer+monomer; purple at  $0.047$  eV:  $3\text{-Li}_{(2,2,2)}$  trigonal; orange: di-Li bound compound. Colors are propagated throughout the activation energy and the final state histograms.

an activation energy of  $E_a = 0.454$  eV, leading to a global displacement along the  $\langle 110 \rangle$  the direction of  $c = 1.97$  Å and a diffusion time of  $\Delta t = 3.766$   $\mu\text{s}$ . With  $D \approx \frac{c^2}{\Delta t}$ , the diffusivity for the translational process is  $D = 9.74 \times 10^{-11}$   $\text{cm}^2 \text{s}^{-1}$ .

The second process is a three-step move associated with a rotation (Fig. 9): A Li first moves from the ground state to  $3\text{-Li}_{(1,2,3)}$  by crossing an activation energy of  $E_a = 0.476$  eV, the second step involves a symmetrical mechanism from  $3\text{-Li}_{(1,2,3)}$  to  $3\text{-Li}_{(1,2,3)}$  with an activation energy of  $E_a = 0.405$  eV, and the last steps bring the system back into GS configuration with an activation energy of  $E_a = 0.463$  eV. The total diffusion corresponds to a  $54.5^\circ$  rotation of the

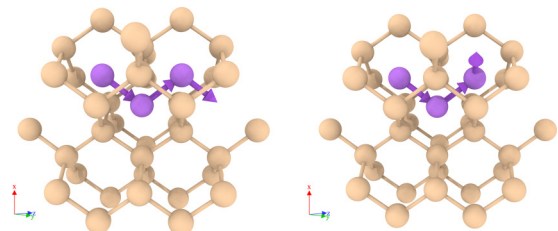


FIG. 9. Representation of the (left) translational and (right) rotational mechanism for the 3-Li system. Li and Si atoms are displayed in purple and beige. The purple arrow points to the displacement of Li atoms throughout the entire mechanism.

trimer from one  $\langle 110 \rangle$  plane to another, leading to a global displacement along the  $\langle 331 \rangle$  direction of  $c = 1.50 \text{ \AA}$  and a diffusion time of  $\Delta t = 4.83 \text{ \mu s}$ . With  $D \approx \frac{c^2}{\Delta t}$ , the diffusivity for the rotational process is  $D = 4.65 \times 10^{-11} \text{ cm}^2 \text{ s}^{-1}$ . While a transition from the GS to 3-Li $_{(2,2,2)}$  trigonal conformation is also shown in Table IV, with a 0.385 eV activation energy, this move does not lead to diffusion but to an oscillation with a 0.54  $\mu\text{s}$  characteristic time at 300 K.

Taken together, the diffusivity for the 3-Li bound compound is  $D = 1.3 \times 10^{-14} \text{ cm}^2 \text{ s}^{-1}$ , two orders of magnitude lower than for the 1-Li and four orders of magnitude lower than the 2-Li. This species contributes therefore very little to the mass transfer. Its lifetime establishes whether it is also a trapping state.

The tri-Li bound compound is defined as the collection of 3-Li $_{(1,1,2)}$ , 3-Li $_{(1,2,5)}$ , 3-Li $_{(2,2,2)}$  tetragonal, and 3-Li $_{(1,2,3)}$  states with associated exiting states presented in Table IV, corresponding to an average lifetime for the tri-Li bound compound of 1.6  $\mu\text{s}$ , significantly lower than the average fastest diffusion time (translation mechanism) of 3.8  $\mu\text{s}$  for this system. The tri-Li bound compound will therefore break before diffusing at 300 K.

#### E. 4 Li atoms

A k-ART simulation is launched from the initial structure with the four Li atoms placed as a compact state where one Li atom is surrounded by the three others in first neighbor position. The simulation runs for 510 KMC steps, representing 1.7 ms of simulation time. After the first KMC step, the tetramer ground state is reached from the initial structure with an activation energy of 0.28 eV by a first nearest-neighbor jump, decreasing the energy by 0.08 eV. The tetramer ground state is described as four 2NN Li atoms forming a tetrahedron with an empty available interstitial site in its center. Its formation and binding energies are  $E_f^{\text{tetramer}} = -4.082 \text{ eV}$  and  $E_b^{\text{tetramer}} = -0.190 \text{ eV}$ , respectively (see Table V).

K-ART finds two transitions from the ground state and four from the compact state. The first transition from the ground state leads back to the compact state with a 0.36 eV activation energy. The second transition from the ground state

TABLE V. Details of formation, binding, and activation energies for the four Li-atom system, including formation and binding energies ( $E_f$ ,  $E_b$ ) and, in the bottom part, the activation energies for pathways between the six dominant states for the Li tetra-Li complex. Multiplicity of transition are values in parenthesis. Energies are in eV.

From \ To	4Li	4Li				
		compact	4Lib	4Lic1	4Lic2	4Lic3
$E_f$	-4.082	-4.002	-4.012	-4.012	-4.012	-4.012
$E_b$	-0.190	-0.110	-0.120	-0.120	-0.120	-0.120
4Li		0.28 (1)	0.52 (1)			
4Li	0.36 (4)			0.47 (1)	0.47 (1)	0.47 (1)
compact						
4Lib	0.59 (12)			(1)	(1)	(1)
4Lic1		0.46 (3)	(1)			
4Lic2		0.46 (3)	(1)			
4Lic3		0.46 (3)	(1)			

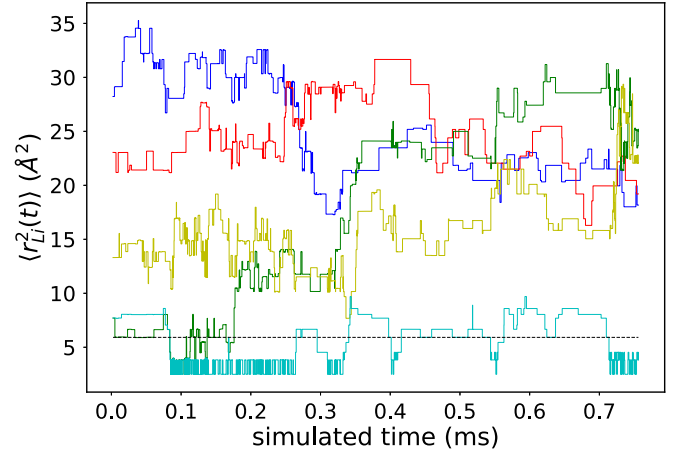


FIG. 10. Evolution of distance between 5 Li pairs out of 45 for the 10-Li system as a function of simulated time. The horizontal dashed black corresponds to the 5th NN distance (5.92  $\text{\AA}$ ).

is associated with 1NN jump on different available empty sites with activation energies of 0.59 eV and a multiplicity of 12 events (i.e., three for each Li atom). This transition breaks the tetramer by pulling a Li atom away from the cluster, to a state at 0.07 eV above, 0.01 eV lower than the compact state.

The first transition from the compact state that leads to the ground state as already been mentioned. The three other transitions break the compact state with degenerate activation energy of 0.46 eV and reduce the energy by 0.01 eV. This activation energy determines the 4-Li bound compound, defined by the ground state and the compact state, with an average calculated lifetime of 1.6  $\mu\text{s}$ .

With a lowest activation energy to break the 4-Li bound compound at 0.46 eV, this compound, as for smaller Li clusters, is short lived. Its low binding energy with respect to dimers of  $E_f^{\text{tetramer}} - 2E_f^{\text{dimer}} = -0.07 \text{ eV}$  is not sufficient to overcome the configurational entropic cost of assembling the four Li. Indeed, in the 4-Li simulation, the bound state breaks at KMC step 111, after 1.4  $\mu\text{s}$ , and is never revisited.

#### F. 10 Li atoms

To assess the interaction between various clusters, the final system we consider consists of 10 Li initially distant from each other in the Si crystalline box. This system is run for 993 KMC steps representing 0.76 ms of simulation time. The lowest energy configuration, reached for the first time at KMC step 253 in 0.14 ms, consists of a trimer, a dimer, and five monomers. The distance between the trimer and the dimer is 13.7  $\text{\AA}$ , the closest monomer to the trimer is at 12.83  $\text{\AA}$ . Its formation energy is  $E_f^{10\text{-Li}} = -9.88 \text{ eV}$ , corresponding to a binding energy of  $E_b^{10\text{-Li}} = -0.15 \text{ eV}$ , represents mostly the sum of the trimer and dimer binding energies. The evolution of a subset of 5 Li-pair distances (out of 45) is shown in Fig 10; the two pairs in first or second nearest neighbor around 0.14 ms are associated with the trimer.

K-ART identifies 1506 topologies and visits 284 of them during the simulation. From Fig. 11, which provides the energy distribution for the various states visited during the simulation, we see that the energy spectrum of the accessible

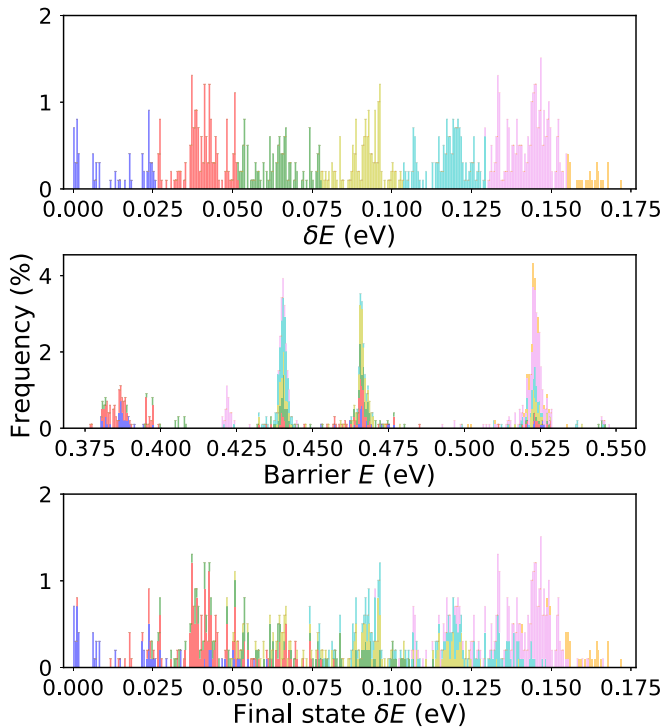


FIG. 11. Evolution of the 10-Li system during the 993 KMC steps. Top panel: energy histogram for the initial states with  $\delta E$  measured from the ground state set at 0.0 eV. Middle panel: histogram of the corresponding activation energies. Bottom panel: energy histogram of the final states. Initial states are color coded with colors assigned based on initial energy. Colors are propagated throughout the activation energy and the final state histograms.

states becomes denser than for previous systems, as activation energies are affected by elastic deformations, even if these are weak. These long-range effects are not sufficient to attract Li into large clusters: Over the 0.76 ms simulation, k-ART recovers the entire catalog of events from the three previous systems (i.e., mono-Li, di-Li, and tri-Li) but the system does not visit states associated with the 4-Li or larger clusters.

#### IV. DISCUSSION AND CONCLUSIONS

The Si matrix can absorb a high concentration of Li, making it a potential candidate for anodes [1–3], although the volume expansion associated with structural transition makes it challenging to use in applications [5,9,10]. To understand this large capacity, we characterize here the energy landscape at relatively low concentrations of Li impurities in *c*-Si using the kinetic activation-relaxation technique coupled with the

reactive force field (ReaxFF) developed by Fan *et al.* [27], an approach that allows the construction of a detailed picture of the first steps of insertion of Li in this material.

K-ART recovers the basic migration energy of the mono-Li interstitial already identified in previous work in addition to finding a number of other transitions such as the IV-pair formation in first or second neighbor position with respect to the Li atom with activation energy of 2.00 eV and 2.29 eV, respectively. After characterizing the energy landscape of Li in substitutional and antisite configurations, we turn our attention to small Li clusters.

Li atoms that first move in silicon, therefore, do not see each other and fail to aggregate into trapped states: Small clusters display only very weak stability and rapidly break apart as they are formed. As more Li atoms are added to the box, we find that these impurities interact only very lightly between themselves: Two, three, and four Li clusters, for example, have lifetimes of only 65.3, 1.6, and 1.6  $\mu$ s, respectively, at 300 K. Since lifetimes for bound compound of three- and four-lithium cluster are considerably smaller than for dimer, large clusters are unlikely to grow even at relatively high Li concentration, ensuring full and uniform packing which explains experimental observations [2,53,54]. Although weak, it could be sufficient, however, to favor clustering and the transition to the high Li-concentrated phase observed experimentally at the anode surface.

Our results provide an essential microscopic and kinetic picture for the onset of Li insertion into Si. They form a solid basis for pursuing the characterization of this system's evolution as Li concentration leads to structural transformation of the underlying structure, contributing valuable information towards the complete understanding of this fascinating complex.

#### V. CODE AVAILABILITY

Various ART nouveau implementations are available freely for download from <http://normandmousseau.com>. The k-ART code is available from the authors upon request.

#### ACKNOWLEDGMENTS

This work was supported in part by grants from the Natural Sciences and Engineering Research Council of Canada (NSERC) and the Université de Montréal. We are grateful to Calcul Québec and Compute Canada for generous allocations of computer resources. We are grateful to A. Stukowski for his powerful OVITO software [55] that facilitated the analysis and illustrations of atomics configurations presented in this paper. OVITO is available at <http://ovito.org/>.

- [1] R. A. Sharma, Thermodynamic properties of the lithium-silicon system, *J. Electrochem. Soc.* **123**, 1763 (1976).
- [2] B. A. Boukamp, All-solid lithium electrodes with mixed-conductor matrix, *J. Electrochem. Soc.* **128**, 725 (1981).
- [3] M. Winter and J. O. Besenhard, Electrochemical lithiation of tin and tin-based intermetallics and composites, *Electrochim. Acta* **45**, 31 (1999).

- [4] C. Julien, A. Mauger, A. Vijn, and K. Zaghib, Lithium batteries, in *Lithium Batteries* (Springer, Cham, 2016), pp. 29–68.
- [5] L. Y. Beaulieu, K. W. Eberman, R. L. Turner, L. J. Krause, and J. R. Dahn, Colossal reversible volume changes in lithium alloys, *Electrochem. Solid-State Lett.* **4**, A137 (2001).
- [6] M. T. McDowell, S. W. Lee, W. D. Nix, and Y. Cui, 25th anniversary article: Understanding the lithiation of silicon and

- other alloying anodes for lithium-ion batteries, *Adv. Mater.* **25**, 4966 (2013).
- [7] P. R. Raimann, N. S. Hochgatterer, C. Korepp, K. C. Möller, M. Winter, H. Schröttner, F. Hofer, and J. O. Besenhard, Monitoring dynamics of electrode reactions in li-ion batteries by in situ esem, *Ionics (Kiel)*. **12**, 253 (2006).
- [8] S. K. Soni, B. W. Sheldon, X. Xiao, M. W. Verbrugge, D. Ahn, H. Haftbaradaran, and H. Gao, Stress mitigation during the lithiation of patterned amorphous Si islands, *J. Electrochem. Soc.* **159**, A38 (2012).
- [9] K.-L. Lee, J.-Y. Jung, S.-W. Lee, H.-S. Moon, and J.-W. Park, Electrochemical characteristics of a-Si thin film anode for li-ion rechargeable batteries, *J. Power Sources* **129**, 270 (2004).
- [10] M. S. Park, G. X. Wang, H. K. Liu, and S. X. Dou, Electrochemical properties of Si thin film prepared by pulsed laser deposition for lithium ion micro-batteries, *Electrochim. Acta* **51**, 5246 (2006).
- [11] B. Key, R. Bhattacharyya, M. Morcrette, V. Sezne, J.-M. Tarascon, and C. P. Grey, Real-time nmr investigations of structural changes in silicon electrodes for lithium-ion batteries real-time nmr investigations of structural changes in silicon electrodes for lithium-ion batteries, *J. Am. Chem. Soc.* **131**, 9239 (2009).
- [12] B. Key, M. Morcrette, J.-M. Tarascon, and C. P. Grey, Pair distribution function analysis and solid state nmr studies of silicon electrodes for lithium ion batteries: Understanding the (de)lithiation mechanisms, *J. Am. Chem. Soc.* **133**, 503 (2011).
- [13] X. H. Liu, J. W. Wang, S. Huang, F. Fan, X. Huang, Y. Liu, S. Krylyuk, J. Yoo, S. A. Dayeh, A. V. Davydov, S. X. Mao, S. T. Picraux, S. Zhang, J. Li, T. Zhu, and J. Y. Huang, In situ atomic-scale imaging of electrochemical lithiation in silicon, *Nat. Nanotechnol.* **7**, 749 (2012).
- [14] H. Kim, B. Han, J. Choo, and J. Cho, Three-dimensional porous silicon particles for use in high-performance lithium secondary batteries, *Angew. Chemie* **120**, 10305 (2008).
- [15] H. Kim, M. Seo, M.-H. Park, and J. Cho, A critical size of silicon nano-anodes for lithium rechargeable batteries, *Angew. Chemie Int. Ed.* **49**, 2146 (2010).
- [16] C. K. Chan, H. Peng, G. Liu, K. McIlwrath, X. F. Zhang, R. A. Huggins, and Y. Cui, High-performance lithium battery anodes using silicon nanowires, *Nat. Nanotechnol.* **3**, 31 (2008).
- [17] C. K. Chan, R. Ruffo, S. S. Hong, R. A. Huggins, and Y. Cui, Structural and electrochemical study of the reaction of lithium with silicon nanowires, *J. Power Sources* **189**, 34 (2009).
- [18] L.-F. Cui, R. Ruffo, C. K. Chan, H. Peng, and Y. Cui, Crystalline-amorphous core-shell silicon nanowires for high capacity and high current battery electrodes, *Nano Lett.* **9**, 491 (2009).
- [19] S. Bourderau, T. Brousse, and D. M. Schleich, Amorphous silicon as a possible anode material for li-ion batteries, *J. Power Sources* **81-82**, 233 (1999).
- [20] S. Ohara, J. Suzuki, K. Sekine, and T. Takamura, A thin film silicon anode for li-ion batteries having a very large specific capacity and long cycle life, *J. Power Sources* **136**, 303 (2004).
- [21] T. L. Kulova, A. M. Skundin, Yu. V. Pleskov, E. I. Terukov, and O. I. Kon'kov, Lithium insertion into amorphous silicon thin-film electrodes, *J. Electroanal. Chem.* **600**, 217 (2007).
- [22] V. Baranchugov, E. Markevich, E. Pollak, G. Salitra, and D. Aurbach, Amorphous silicon thin films as a high capacity anodes for li-ion batteries in ionic liquid electrolytes, *Electrochem. commun.* **9**, 796 (2007).
- [23] J.-F. Joly, L. K. Béland, P. Brommer, and N. Mousseau, Contribution of vacancies to relaxation in amorphous materials: A kinetic activation-relaxation technique study, *Phys. Rev. B* **87**, 144204 (2013).
- [24] L. K. Béland, Y. Anahory, D. Smeets, M. Guihard, P. Brommer, J.-F. Joly, J.-C. Pothier, L. J. Lewis, N. Mousseau, and F. Schiettekatte, Replenish and Relax: Explaining Logarithmic Annealing in Ion-Implanted c-Si, *Phys. Rev. Lett.* **111**, 105502 (2013).
- [25] P. Brommer, L. K. Béland, J.-F. Joly, and N. Mousseau, Understanding long-time vacancy aggregation in iron: A kinetic activation-relaxation technique study, *Phys. Rev. B* **90**, 134109 (2014).
- [26] M. Trochet, L. K. Béland, J.-F. Joly, P. Brommer, and N. Mousseau, Diffusion of point defects in crystalline silicon using the kinetic activation-relaxation technique method, *Phys. Rev. B* **91**, 224106 (2015).
- [27] F. Fan, S. Huang, H. Yang, M. Raju, D. Datta, V. B. Shenoy, A. C. T. van Duin, S. Zhang, and T. Zhu, Mechanical properties of amorphous li x Si alloys: A reactive force field study, *Model. Simul. Mater. Sci. Eng.* **21**, 074002 (2013).
- [28] F. El-Mellouhi, N. Mousseau, and L. J. Lewis, Kinetic activation-relaxation technique: An off-lattice self-learning kinetic monte carlo algorithm, *Phys. Rev. B* **78**, 153202 (2008).
- [29] L. K. Béland, P. Brommer, F. El-Mellouhi, J.-F. Joly, and N. Mousseau, Kinetic activation-relaxation technique, *Phys. Rev. E* **84**, 046704 (2011).
- [30] A. B. Bortz, M. H. Kalos, and J. L. Lebowitz, A new algorithm for monte carlo simulation of ising spin systems, *J. Comput. Phys.* **17**, 10 (1975).
- [31] A. F. Voter, *Radiation Effects in Solids NATO Science Series (Introduction to the kinetic Monte Carlo method)* (Springer, Dordrecht, 2007).
- [32] B. D. McKay, Practical graph isomorphism, *Congr. Numer.* **30**, 4587 (1981).
- [33] G. T. Barkema and N. Mousseau, Event-Based Relaxation of Continuous Disordered Systems, *Phys. Rev. Lett.* **77**, 4358 (1996).
- [34] R. Malek and N. Mousseau, Dynamics of Lennard-Jones clusters: A characterization of the activation-relaxation technique, *Phys. Rev. E* **62**, 7723 (2000).
- [35] J.-F. Joly, L. K. Béland, P. Brommer, F. El-Mellouhi, and N. Mousseau, Optimization of the kinetic activation-relaxation technique, an off-lattice and self-learning kinetic monte-carlo method, *J. Phys. Conf. Ser.* **341**, 012007 (2012).
- [36] N. Mousseau, L. K. Béland, P. Brommer, J.-F. Joly, F. El-Mellouhi, E. Machado-Charry, M.-C. Marinica, and P. Pochet, The activation-relaxation technique: Art nouveau and kinetic art, *J. At. Mol. Opt. Phys.* **2012**, 1 (2012).
- [37] N. Mousseau, L. K. Béland, P. Brommer, F. El-Mellouhi, J.-F. Joly, G. K. N'Tsouaglo, O. Restrepo, M. Trochet, and L. K. B., Following atomistic kinetics on experimental timescales with the kinetic activation-relaxation technique, *Comput. Mater. Sci.* **100**, 111 (2014).
- [38] M. Trochet, A. Sauvé-Lacoursière, and N. Mousseau, Algorithmic developments of the kinetic activation-relaxation technique: accessing long-time kinetics of larger and more complex systems, *J. Chem. Phys.* **147**, 152712 (2017).
- [39] E. Machado-Charry, L. K. Béland, D. Caliste, L. Genovese, T. Deutsch, N. Mousseau, and P. Pochet, Optimized energy

- landscape exploration using the ab initio based activation-relaxation technique, *J. Chem. Phys.* **135**, 034102 (2011).
- [40] B. Puchala, M. L. Falk, and K. Garikipati, An energy basin finding algorithm for kinetic monte carlo acceleration, *J. Chem. Phys.* **132**, 134104 (2010).
- [41] S. Plimpton, Fast parallel algorithms for short-range molecular dynamics, *J. Comput. Phys.* **117**, 1 (1995).
- [42] A. C. T. van Duin, S. Dasgupta, F. Lorant, and W. A. Goddard, Reaxff: A reactive force field for hydrocarbons, *J. Phys. Chem. A* **105**, 9396 (2001).
- [43] C. Kittel, *Introduction to Solid State Physics*, 8th ed. (Wiley, New York, 2005).
- [44] L. T. Canham, *Properties of Silicon, EMIS Datareviews Series No. 4* (INSPEC, London, 1987), pp. 454–462.
- [45] O. I. Malys, T. L. Tan, and S. Manzhos, A comparative computational study of structures, diffusion, and dopant interactions between li and na insertion into Si, *Appl. Phys. Express* **6**, 027301 (2013).
- [46] W. Wan, Q. Zhang, Y. Cui, and E. Wang, First principles study of lithium insertion in bulk silicon, *J. Phys. Condens. Matter* **22**, 415501 (2010).
- [47] A. J. Morris, R. J. Needs, E. Salager, C. P. Grey, and C. J. Pickard, Lithiation of silicon via lithium zintl-defect complexes from first principles, *Phys. Rev. B* **87**, 174108 (2013).
- [48] A. Ostadhosseini, E. D. Cubuk, G. A. Tritsarlis, E. Kaxiras, S. Zhang, and A. C. T. van Duin, Stress effects on the initial lithiation of crystalline silicon nanowires: Reactive molecular dynamics simulations using reaxff, *Phys. Chem. Phys.* **17**, 3832 (2015).
- [49] H. Kim, K. E. Kweon, C. Y. Chou, J. G. Ekerdt, and G. S. Hwang, On the nature and behavior of li atoms in Si: A first principles study, *J. Phys. Chem. C* **114**, 17954 (2010).
- [50] W.-K. Leung, R. J. Needs, G. Rajagopal, S. Itoh, and S. Ihara, Calculations of Silicon Self-Interstitial Defects, *Phys. Rev. Lett.* **83**, 2351 (1999).
- [51] L. A. Marqués, L. Pelaz, J. Hernández, J. Barbolla, and G. H. Gilmer, Stability of defects in crystalline silicon and their role in amorphization, *Phys. Rev. B* **64**, 045214 (2001).
- [52] F. Cargnoni, C. Gatti, and L. Colombo, Formation and annihilation of a bond defect in silicon: An ab initio quantum-mechanical characterization, *Phys. Rev. B* **57**, 170 (1998).
- [53] C. S. Fuller and J. C. Severiens, Mobility of impurity ions in germanium and silicon, *Phys. Rev.* **96**, 21 (1954).
- [54] M. J. Chon, V. A. Sethuraman, A. McCormick, V. Srinivasan, and P. R. Guduru, Real-Time Measurement of Stress and Damage Evolution During Initial Lithiation of Crystalline Silicon, *Phys. Rev. Lett.* **107**, 045503 (2011).
- [55] A. Stukowski, Visualization and analysis of atomistic simulation data with ovito the open visualization tool, *Model. Simul. Mater. Sci. Eng.* **18**, 015012 (2010).